

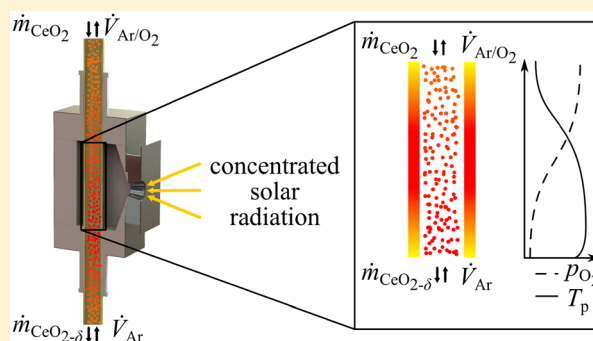
# Experimental Demonstration of the Thermochemical Reduction of Ceria in a Solar Aerosol Reactor

Michael Welte,<sup>†</sup> Rafik Barhoumi,<sup>†</sup> Adrian Zbinden,<sup>†</sup> Jonathan R. Scheffe,<sup>‡</sup> and Aldo Steinfeld<sup>\*,†</sup>

<sup>†</sup>Department of Mechanical and Process Engineering, ETH Zürich, 8092 Zürich, Switzerland

<sup>‡</sup>Department of Mechanical and Aerospace Engineering, University of Florida, Gainesville, Florida 32611-6250, United States

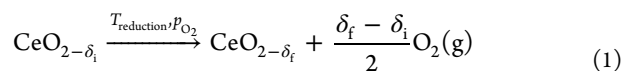
**ABSTRACT:** We report on the experimental demonstration of an aerosol solar reactor for the thermal reduction of ceria, as part of a thermochemical redox cycle for splitting H<sub>2</sub>O and CO<sub>2</sub>. The concept utilizes a cavity-receiver enclosing an array of alumina tubes, each containing a downward gravity-driven aerosol flow of ceria particles countercurrent to an inert sweep gas flow for intrinsic separation of reduced ceria and oxygen. A 2 kW<sub>th</sub> lab-scale prototype with a single tube was tested under radiative fluxes approaching 4000 suns, yielding reaction extents of up to 53% of the thermodynamic equilibrium at 1919 K within residence times below 1 s. Upon thermal redox cycling, fresh primary particles of 2.44 μm mean size initially formed large agglomerates of 1000 μm mean size, then sintered into stable particles of 150 μm mean size. The reaction extent was primarily limited by heat transfer for large particles/agglomerates (mean size > 200 μm) and by the gas phase advection of product O<sub>2</sub> for smaller particles.



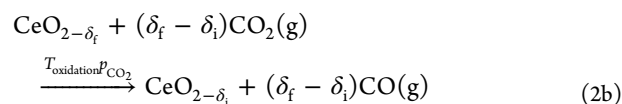
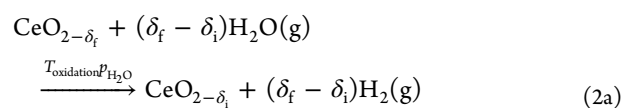
## 1. INTRODUCTION

Thermochemical cycles based on metal oxide redox reactions are capable of splitting H<sub>2</sub>O and/or CO<sub>2</sub> into H<sub>2</sub> and/or CO using concentrated solar energy.<sup>1,2</sup> Nonstoichiometric ceria is currently considered the benchmark among the nonvolatile redox materials because of its rapid kinetics and crystallographic stability.<sup>3–6</sup> The two-step cycle proceeds according to the following reactions:

Reduction



Oxidation:



During the first solar-driven endothermic step (eq 1), ceria is thermally reduced at temperatures generally above 1573 K using solar process heat. The equilibrium reduction extent, given by the final nonstoichiometry  $\delta_f$ , is dependent on the reduction temperature  $T_{\text{reduction}}$  and the oxygen partial pressure  $p_{\text{O}_2}$  of the surrounding gas atmosphere.<sup>7</sup> Following reduction, the reduced ceria is reoxidized to its initial nonstoichiometry  $\delta_i$  with H<sub>2</sub>O (eq 2a) and/or CO<sub>2</sub> (eq 2b) to form H<sub>2</sub> and/or CO

at an oxidation temperature  $T_{\text{oxidation}}$  generally lower than 1273 K. Several solar reactor concepts have been proposed for performing the redox cycle with nonvolatile metal oxides. These include a circulating fluidized bed for the reduction of NiFe<sub>2</sub>O<sub>4</sub>/m-ZrO<sub>2</sub> particles,<sup>8</sup> which offers good heat transfer and kinetics due to small particles while the window imposes a limitation on the scale-up potential, a counter-rotating set of rings for reducing Fe<sub>3</sub>O<sub>4</sub> or CeO<sub>2</sub> that enables solid–solid heat recovery,<sup>9,10</sup> a similar rotary-type reactor for reducing CeO<sub>2</sub> or Ni–Mn–ferrite (Ni<sub>0.5</sub>Mn<sub>0.5</sub>Fe<sub>2</sub>O<sub>4</sub>) that alternates between reduction and oxidation,<sup>11</sup> and a rotating cylinder made from porous CeO<sub>2</sub> with an additional inert counter rotating cylinder on the inside for heat recovery.<sup>12</sup> All of these concepts benefit from the implemented solid–solid heat recovery and are able to produce a continuous fuel output, while facing the challenge of a window and moving reactor component at high operating temperatures. A cylindrical cavity containing an array of tubular reactive elements operated isothermally in batch or continuous mode inherently avoids the need for solid–solid heat recuperation but is limited to low fuel concentrations introducing additional downstream processes.<sup>13</sup> A moving packed bed of ceria particles incorporating solid–solid heat recovery and pressure separation of reduction and oxidation zones was proposed, which has the potential to decouple the reduction from the oxidation.<sup>14</sup> An additional concept is a

**Received:** July 26, 2016

**Revised:** September 19, 2016

**Accepted:** September 23, 2016

**Published:** September 23, 2016

cavity-receiver lined with porous ceria monoliths or felts.<sup>15,16</sup> The latter was also tested with a reticulated porous structure made of ceria for enhanced heat and mass transfer, reaching a solar-to-fuel energy conversion efficiency of 1.73% (without heat recovery).<sup>17,18</sup> Recently, we proposed a novel solar reactor concept based on a cavity-receiver enclosing an array of alumina tubes, each containing a downward aerosol flow of ceria particles counter to an inert sweep gas flow.<sup>19</sup> Owing to the countercurrent arrangement of the particle and gas flows, the local  $p_{\text{O}_2}$  gradually decreases while the particle temperature increases, resulting in an intrinsic separation of the reduced metal oxide from the produced oxygen. This separation is critical to avoid recombination. Furthermore, this concept offers enhanced heat and mass transfer, good scalability because of the modular multiple-tube configuration, and can be operated isothermally and continuously, thus decoupling the two redox steps both in space and time for round-the-clock fuel production.<sup>20,21</sup> The disadvantages are associated with the complexity of handling large flows of particles across the hot reaction zone in short residence times, and the limitations imposed by the materials of construction of the solar tubular absorber such as the maximum operating temperature, thermal conductivity, resistance to thermal shocks, and inertness to oxidation by air.

In this work, we report on the experimental performance of a solar aerosol reactor prototype fabricated with a single tube and tested for the first time under realistic concentrated radiation conditions. Additionally, we study the effect of cycling on the particle morphology and the subsequently measured reduction extent, and elucidate the dominant controlling mechanisms via heat and mass transfer modeling.

## 2. EXPERIMENTAL METHODS

The solar reactor is schematically depicted in Figure 1. It consists of a vertical  $\text{Al}_2\text{O}_3$  tube (Haldenwanger, ALSINT 99.7,  $D_{\text{out}} = 50$  mm,  $D_{\text{in}} = 42$  mm,  $L = 850$  mm) which withstands the high operating temperatures and it is inert to air. The tube is positioned inside a cavity-receiver ( $200 \times 86 \times 86$  mm<sup>3</sup>) lined with 40 mm-thick alumina/silica based insulation (65%

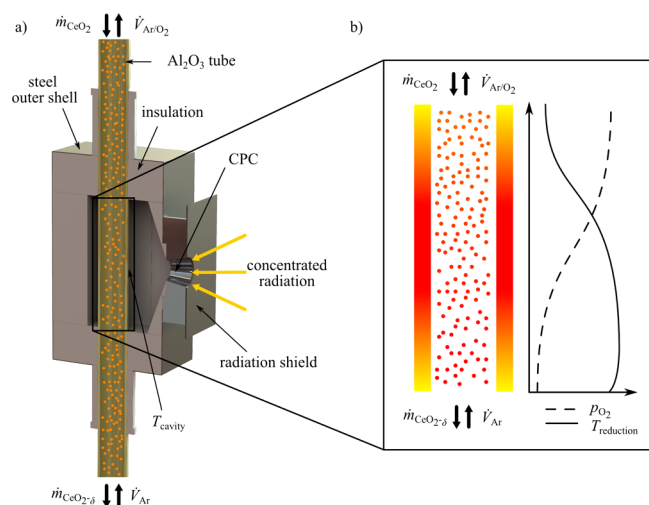


**Figure 1.** (a) Schematic of the solar receiver indicating the main components and material flows. (b) Scheme of the reaction zone alongside qualitative profiles of the particle temperature  $T_{\text{reduction}}$  and oxygen partial pressure  $p_{\text{O}_2}$ .

$\text{Al}_2\text{O}_3$ , 35%  $\text{SiO}_2$ , Insulform 1600) and supported by a stainless steel shell. Concentrated solar radiation enters the windowless cavity through its 30 mm-diameter circular aperture. Because of multiple internal reflections and absorptions, the cavity approaches a blackbody absorber and efficiently captures the incoming concentrated solar radiation as high-temperature heat. A refrigerated polished-Al compound parabolic concentrator (CPC) of 45° half acceptance angle is incorporated at the aperture to boost the solar concentration ratio and mitigate reradiation losses.<sup>22,23</sup> Ceria particles ( $D_{\text{v50}} = 70$   $\mu\text{m}$ , Chempur, 99.9% purity) were supplied to the top of the alumina tube by a particle feeder featuring an adjustable orifice operated by an electrical motor (Micro motors E192.24.25) and carried to the reaction zone by gravity. At the bottom of the alumina tube, the particles were collected on a balance (Mettler Toledo XS1003S) for online measurement of the ceria mass flow rate  $\dot{m}_{\text{CeO}_2}$ . Argon purge gas was delivered upward through the balance housing and downward through the feeder by electronic mass flow controllers (Bronkhorst, F-201CV and F-201C). Gases exited through a lateral outlet above the reaction zone shortly below the feeder and were analyzed online using a mass spectrometer (MS, Pfeiffer Vacuum, OmniStar GSD 320) and an electrochemical-based oxygen sensor (Setnag, trace oxygen analyzer JC24 V-R). The residual oxygen partial pressure  $p_{\text{O}_2, \text{baseline}}$  within the system was measured prior to an experiment. The nominal cavity temperature  $T_{\text{cavity}}$  was measured by a type-B thermocouple located at the front of the alumina tube. Because of multiple internal absorptions, reflections, and re-emissions by the inner cavity walls, no large temperature gradients were expected. The particle temperature, which increased from ambient to its maximum value before exiting the hot reaction zone, was not measured. Thus,  $T_{\text{cavity}}$  set an upper limit for the actual particle-flow temperature. The reduction extent was calculated using the measured values of  $\dot{m}_{\text{CeO}_2}$  and  $p_{\text{O}_2}$ . Prior to each experimental run, reduced particles from the previous experiment were exposed to air at 573 K for more than 8 h to ensure a fully oxidized state ( $\delta_1 = 0$ ), as verified by thermogravimetric analysis. Experiments were performed at the High-Flux Solar Simulator (HFSS) of ETH Zurich: an array of seven Xe arcs, close-coupled to truncated ellipsoidal specular reflectors, provided an external source of intense thermal radiation, mostly in the visible and IR spectra, closely approximating the radiative heat transfer characteristics of highly concentrating solar systems such as solar towers and dishes.<sup>24</sup> The radiative power input  $P_{\text{solar}}$  was determined optically with a calibrated CCD camera and verified by calorimeter measurements.

During a typical solar experimental run, the cavity-receiver was heated by concentrated radiation delivered by the HFSS to the desired  $T_{\text{cavity}}$  as high as 1919 K. The radiative power input was in the range  $P_{\text{solar}} = 2.28$ –2.8 kW, resulting in mean solar concentration ratios over the aperture in the range 3226–3954 suns (1 sun = 1 kW m<sup>-2</sup>). A constant argon flow was delivered at a rate  $\dot{V}_{\text{Ar}}$  in the range of 2–4 L min<sup>-1</sup> (SLPM, gas flow rates calculated at 273.15 K and 101 325 Pa) through the tube and 0.1 L min<sup>-1</sup> through the feeder. Residual oxygen concentrations were below 200 ppmv. Once approximate isothermal conditions were reached, a constant  $\dot{m}_{\text{CeO}_2}$  was supplied from the top. An electrically heated setup (Carbolite, STF 16/-/450) was also used to assess key operational parameters under more controlled conditions and a longer heated section of the tube. The electric setup was previously described, and its key features

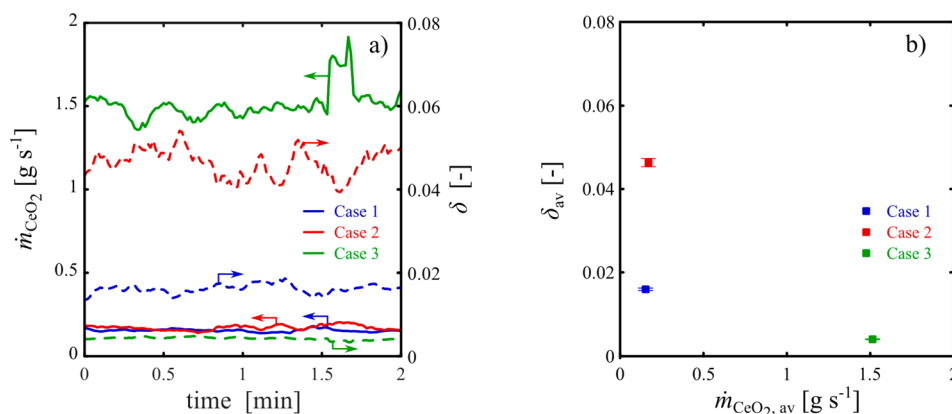


**Figure 2.** (a) Temporal evolution of ceria mass flow rates and corresponding reduction extents for three solar experimental runs. (b) Average reduction extents as a function of average ceria mass flow rate. Error bars indicate the 95% confidence interval. Operating conditions: Case 1) (baseline)  $\dot{m}_{\text{CeO}_2} = 0.15 \text{ g s}^{-1}$ ,  $\dot{V}_{\text{Ar}} = 2 \text{ L min}^{-1}$ ,  $P_{\text{solar}} = 2.28 \text{ kW}$ ,  $T_{\text{cavity}} = 1902 \text{ K}$ ; Case 2)  $\dot{m}_{\text{CeO}_2} = 0.17 \text{ g s}^{-1}$ ,  $\dot{V}_{\text{Ar}} = 4 \text{ L min}^{-1}$ ,  $P_{\text{solar}} = 2.28 \text{ kW}$ ,  $T_{\text{cavity}} = 1919 \text{ K}$ ; Case 3)  $\dot{m}_{\text{CeO}_2} = 1.5 \text{ g s}^{-1}$ ,  $\dot{V}_{\text{Ar}} = 2 \text{ L min}^{-1}$ ,  $P_{\text{solar}} = 2.80 \text{ kW}$ ,  $T_{\text{cavity}} = 1886 \text{ K}$ . For all three cases,  $p_{\text{O}_2, \text{baseline}} = 2 \times 10^{-4} \text{ atm}$ .

**Table 1.** Operating Conditions and Main Results of the Three Solar Experimental Runs of Figure 2

case	$\dot{m}_{\text{CeO}_2}$ [ $\text{g s}^{-1}$ ]	$\dot{V}_{\text{Ar}}$ [ $\text{L min}^{-1}$ ]	$T_{\text{cavity}}$ [K]	$P_{\text{solar}}$ [kW]	$\delta$ [-]	$\eta_{\text{solar-to-fuel}}$ [%]
1	$0.15 \pm 0.0015^b$	2	$1902 \pm 8^a$	2.28	$0.0162 \pm 0.0004^b$	0.18
2	$0.17 \pm 0.0026$	4	$1919 \pm 8$	2.28	$0.0463 \pm 0.0012$	0.56
3	$1.50 \pm 0.0167$	2	$1886 \pm 8$	2.80	$0.0042 \pm 0.0001$	0.37

<sup>a</sup>Given by manufacturer. <sup>b</sup>95% confidence interval.

are summarized here.<sup>19</sup> Similar to the solar reactor, it also featured a single alumina tube, but of dimensions  $D_{\text{out}} = 25.4 \text{ mm}$ ,  $D_{\text{in}} = 19.1 \text{ mm}$ ,  $L = 1300 \text{ mm}$ . For both setups, ceria particles ( $D_{\text{v50}} = 2.44 \text{ }\mu\text{m}$ , Sigma-Aldrich, 99.9% purity) were fed at an  $\dot{m}_{\text{CeO}_2}$  of up to  $0.7 \text{ g s}^{-1}$  for at least 60 s. Particle morphology was characterized by scanning electron microscopy (SEM, Hitachi TM-1000), and particle size distribution was analyzed by laser scattering (Horiba LA-950) and image processing software (ImageJ v1.48). Particle sieves were used to control their size distribution.

### 3. RESULTS AND DISCUSSION

**Solar Experimentation.** The steady-state ceria mass flow rate and the corresponding reduction extent are shown in Figure 2. Figure 2a as a function of time for three operating conditions (cases 1–3), while the corresponding average values are summarized in Table 1 and shown in Figure 2b. Error bars indicate the 95% confidence interval. Operating conditions were as follows. Case 1 (baseline):  $\dot{m}_{\text{CeO}_2} = 0.15 \text{ g s}^{-1}$ ,  $\dot{V}_{\text{Ar}} = 2 \text{ L min}^{-1}$ ,  $P_{\text{solar}} = 2.28 \text{ kW}$ ,  $T_{\text{cavity}} = 1902 \text{ K}$ . Case 2:  $\dot{m}_{\text{CeO}_2} = 0.17 \text{ g s}^{-1}$ ,  $\dot{V}_{\text{Ar}} = 4 \text{ L min}^{-1}$ ,  $P_{\text{solar}} = 2.28 \text{ kW}$ ,  $T_{\text{cavity}} = 1919 \text{ K}$ . Case 3:  $\dot{m}_{\text{CeO}_2} = 1.5 \text{ g s}^{-1}$ ,  $\dot{V}_{\text{Ar}} = 2 \text{ L min}^{-1}$ ,  $P_{\text{solar}} = 2.80 \text{ kW}$ ,  $T_{\text{cavity}} = 1886 \text{ K}$ . For all three cases,  $p_{\text{O}_2, \text{baseline}} = 2 \times 10^{-4} \text{ atm}$ . For case 1 (solid lines), the average  $\delta$  measured was 0.0162, which corresponded to a reaction extent of 20% of the thermodynamic equilibrium. Since the equilibrium was calculated based on  $T_{\text{reduction}} = T_{\text{cavity}}$  and  $p_{\text{O}_2, \text{baseline}} = 2 \times 10^{-4} \text{ atm}$ , the value of the reaction extent is a conservative estimate as  $T_{\text{cavity}}$  sets the upper particle temperature limit and  $p_{\text{O}_2, \text{baseline}}$  sets the lower oxygen concentration limit. For case 2 (large dashes), in which the gas flow rate was doubled while the ceria mass flow rate was kept constant within the feeder accuracy,  $\delta$  was almost tripled to 0.0462 with a reaction extent of 53%. For case 3 (small

dashes), in which  $\dot{m}_{\text{CeO}_2}$  was increased by a factor of 10 while  $P_{\text{solar}}$  was increased from 2.28 to 2.8 kW to maintain  $T_{\text{cavity}} > 1873 \text{ K}$ ,  $\delta$  decreased to 0.0042 and the reaction extent reached 6%. Typical residence time in the reaction zone for free falling particles is below 1 s.

The average solar-to-fuel energy conversion efficiency  $\eta_{\text{solar-to-fuel}}$  is defined as

$$\eta_{\text{solar-to-fuel}} = \frac{2\text{HHV}_{\text{H}_2} \int \delta \dot{n}_{\text{CeO}_2} dt}{P_{\text{solar}} + E_{\text{inert}} \int \dot{n}_{\text{inert}} dt} \quad (3)$$

where  $\dot{n}_{\text{CeO}_2}$  is the molar flow rate of ceria,  $\dot{n}_{\text{inert}}$  is the molar flow rate of the inert gas,  $\text{HHV}_{\text{H}_2}$  is the higher heating value of hydrogen (assuming complete oxidation eq 2a) and  $E_{\text{inert}}$  is the energy required to separate the inert gas (assumed  $20 \text{ kJ mol}^{-1}$ ).<sup>25</sup> Sensible heat recovery from the exiting hot particles and gases was not realized in this study. Particles were fed at room temperature instead of the more realistic oxidation temperature, thus resulting in a conservative estimate for the efficiencies. It is further implicitly assumed that complete reoxidation with stoichiometric amounts of  $\text{H}_2\text{O}$  can be achieved, as corroborated experimentally.<sup>26</sup> Results are summarized in Table 1. Overall,  $\eta_{\text{solar-to-fuel}}$  increased with  $\dot{m}_{\text{CeO}_2}$  rate and  $\dot{V}_{\text{Ar}}$ . Specifically,  $\eta_{\text{solar-to-fuel}}$  increased from 0.18 to 0.37% when increasing  $\dot{m}_{\text{CeO}_2}$  from its baseline by a factor of 10, even though  $\delta$  dropped by almost a factor of 4. The drop in  $\delta$  is attributed to radiative heat transfer effects, as a higher  $\dot{m}_{\text{CeO}_2}$  results in a larger extinction coefficient, which in turn results in a lower particle temperature because of the optically thicker medium. An increase of  $\dot{V}_{\text{Ar}}$  from its baseline by a factor of 2 resulted in an increase of  $\eta_{\text{solar-to-fuel}}$  to 0.56% because the local  $p_{\text{O}_2}$  was lower, thus shifting the thermodynamic equilibrium to higher  $\delta$  values at same temperatures. Recycling Ar at these gas

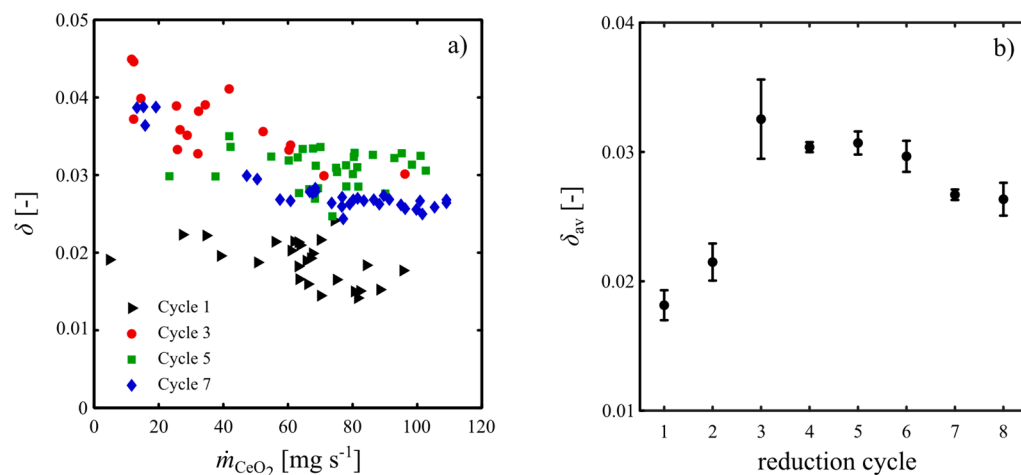


**Figure 3.** (a) Experimentally measured reduction extents as a function of the ceria feeding rate using the electrically heated setup. Experimental conditions:  $\dot{V}_{\text{Ar}} = 0.5 \text{ L min}^{-1}$ ,  $p_{\text{O}_2, \text{baseline}} < 5 \times 10^{-5} \text{ atm}$ ,  $T_{\text{t}} = 1873 \text{ K}$ . (b) Evolution of the mean reduction extent,  $\delta_{\text{av}}$ , over the first eight cycles. Error bars correspond to 95% confidence intervals. Experimental conditions:  $\dot{m}_{\text{CeO}_2} = 50$  and  $120 \text{ mg s}^{-1}$ ,  $\dot{V}_{\text{Ar}} = 0.5 \text{ L min}^{-1}$ ,  $p_{\text{O}_2, \text{baseline}} < 5 \times 10^{-5} \text{ atm}$ ,  $T_{\text{t}} = 1873 \text{ K}$ .

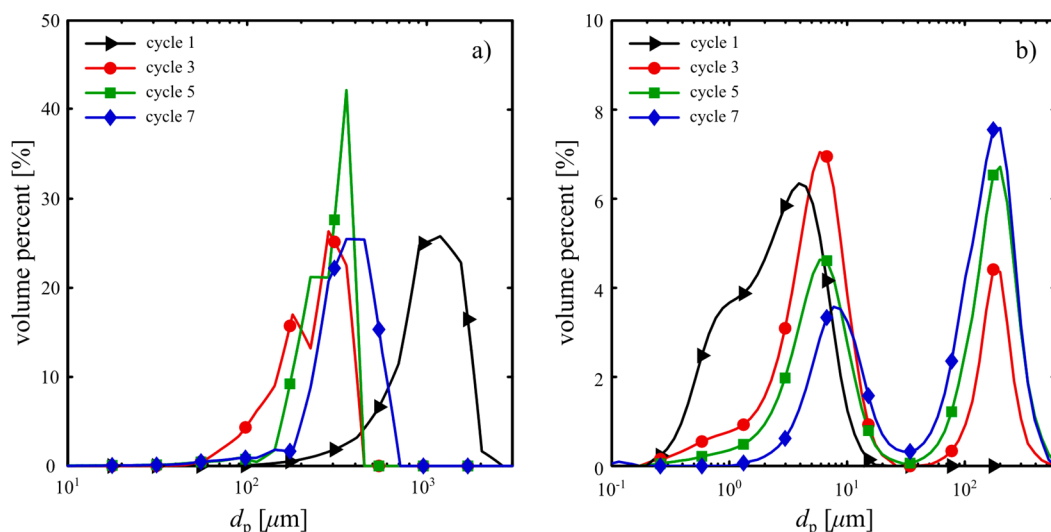


**Figure 4.** Agglomerate sizes obtained from image processing (a) and corresponding primary particle size distributions obtained by laser scattering (b) for cycles 1, 3, 5, and 7.

flow rates requires its separation from  $\text{O}_2$ , which introduces an energy penalty as indicated in eq 3. For our experimental conditions with  $\dot{V}_{\text{Ar}}$  in the range  $2\text{--}4 \text{ L min}^{-1}$ ,  $E_{\text{inert}}/\dot{n}_{\text{inert}} dt = 0.7\text{--}1.3\%$  of  $P_{\text{solar}}$  (2.28 kW).

**Particle Morphology.** To study the effect of repeated cycling on the particle morphology, we subjected a 200 g batch of ceria powder to eight consecutive redox cycles using the electrically heated setup. Each cycle consisted of several individual experiments with varying feeding rates until the entire 200 g batch was exhausted, for a total of 15 experiments per batch carried out at  $T_{\text{t}} = 1873 \text{ K}$ . Results are shown in Figure 3a, where  $\delta$  is plotted as a function of  $\dot{m}_{\text{CeO}_2}$  for cycles 1, 3, 5, and 7.  $\delta$  was generally shown to be inversely proportional to  $\dot{m}_{\text{CeO}_2}$ . For example, in cycle 7,  $\delta$  was 0.039 at  $\dot{m}_{\text{CeO}_2} = 15 \text{ mg s}^{-1}$  and 0.026 at  $\dot{m}_{\text{CeO}_2} = 130 \text{ mg s}^{-1}$ , reaching respectively 42% and 29% of the thermodynamic limit for  $T_{\text{reduction}} = 1873 \text{ K}$  and  $p_{\text{O}_2, \text{baseline}} = 5 \times 10^{-5} \text{ atm}$ . Furthermore,  $\delta$  increased substantially from cycle 1 to 3, but decreased slightly between

cycle 5 and 7. This trend can be seen more clearly in Figure 3b, where average reduction extents  $\delta_{\text{av}}$  are shown versus cycle number for a narrow range of  $\dot{m}_{\text{CeO}_2}$  between 50 and  $120 \text{ mg s}^{-1}$ . The trend is in the direction of decreasing  $\delta$  with subsequent redox cycles. In a previous study using an infrared furnace, ceria was shown to be stable for 500 redox cycles, after an initial stabilization period of about 100 redox cycles.<sup>3</sup>

Image-based particle size distributions measured in their oxidized state revealed the presence of large particle agglomerates. Results are indicated in Figure 4a for cycles 1, 3, 5, and 7. During the first three cycles, the agglomerate size decreased, followed by a small increase during the remaining cycles. This correlates well with the behavior of  $\delta_{\text{av}}$  shown in Figure 3b where larger agglomerates correspond to lower  $\delta_{\text{av}}$ . Laser scattering measurements shown in Figure 4b enable insight on the particle history. Fresh particles are shown to have the smallest size because primary particles were measured rather than agglomerates. Upon cycling, the primary particle size increased and a second peak could be detected at  $\sim 160$

$\mu\text{m}$ . Even though the fraction of these larger particles gradually increased, no further increase in their size was detected. This growth was likely a result of particle agglomerates sintering, ultimately causing a transition from Geldart class C to class A particles.<sup>27</sup> In addition to the size variation between cycles, the agglomerates also exhibited a variation in their surface morphology, as revealed by SEMs in Figure 5 for cycles 1, 3,

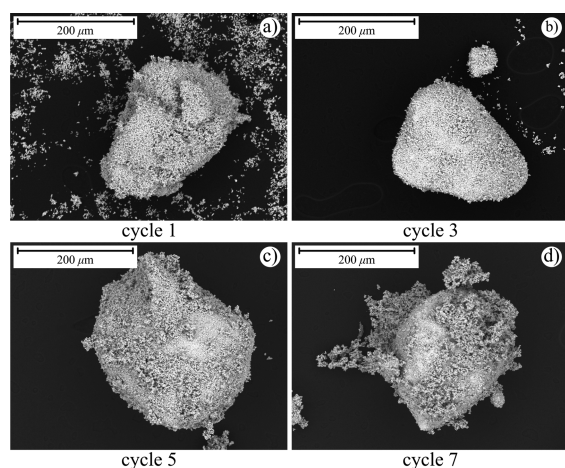


**Figure 5.** SEM images of ceria particles as used during reduction cycles 1, 3, 5, and 7 are shown in panels a, b, c, and d, respectively.

5, and 7. We selected agglomerates of similar size to emphasize their structural differences. During the first three cycles the agglomerates became denser, resulting in smoother surfaces. By cycle 5 these agglomerates were covered with smaller primary particles. This process continued during the remaining cycles, apparently resulting in a porous structure made up of small primary particles (Figure 5d).

**Heat and Mass Transfer Analysis.** A 1-D 2-phase coupled heat and mass transfer model is formulated for the reaction zone consisting of a cylindrical tube section (length  $L_{\text{reac}} = 0.35$  m, diameter  $D_t = 0.191$  m) containing a particle flow at a rate  $\dot{m}_{\text{CeO}_2}$  falling by gravity and countercurrent to an argon flow at a rate  $\dot{V}_{\text{Ar}}$ . The particles were assumed spherical with a surface area  $A_p$ , falling at terminal velocity based on Schiller–Nauman–Drag through a reaction zone.<sup>28</sup> The solid-phase energy balance for the particle stream considered the incoming radiative flux from the hot tube wall, reradiation, and convective heat transfer with the gas phase.<sup>29,30</sup> For simplicity, the reaction enthalpy was neglected as it typically corresponded to less than 11% of the total energy transferred. Because the optical thickness  $\kappa = 0.06$  ( $\ll 1$ ), the near-transparent media approximation was applied. The incident radiative flux was approximated based on the view factor  $F_{t-p}(z)$  to a single particle falling through the tube centerline multiplied by the total radiative flux emitted by the tube wall and the particle concentration  $N$ . Normal total emittance of ceria was taken from literature  $\epsilon_{\text{CeO}_2} = 0.75$ .<sup>31</sup> The total energy incident on the particle becomes independent of the tube wall emittance as a result of the small particle to wall surface ratio. The gas-phase energy balance considered convective heat transfer between gas flow and tube wall and between gas flow and particle stream, with the corresponding heat transfer coefficients  $h_{t-g}$  and  $h_{p-g}$  calculated using  $Nu$  correlations.<sup>29,32</sup> Conduction by particle–particle contact was neglected.<sup>33</sup> Conduction through the particles was neglected as justified by the Biot number  $< 0.07$ .

Note that the gas and particle flows were countercurrent and entered the reaction zone from opposite ends at 300 K. The oxygen source resulted from the change in  $\delta$  for a given  $\dot{m}_{\text{CeO}_2}$ , assuming thermodynamic equilibrium at  $p_{\text{O}_2}$  and  $T_s$ .<sup>26</sup> The governing 1D steady-state energy conservation equations for the solid (particles) and gas phases are

$$\dot{m}_{\text{CeO}_2} c_{p,\text{CeO}_2} \frac{dT_s(z)}{dz} = N \epsilon_{\text{CeO}_2} F_{t-p}(z) A_t \sigma T_t^4 - N \epsilon_{\text{CeO}_2} A_p \sigma T_s^4(z) + N h_{p-g} A_p (T_g(z) - T_s(z)) \quad (4)$$

$$\rho_{\text{Ar}} \dot{V}_g c_{p,\text{Ar}} \frac{dT_g(z)}{dz} = \pi D_t h_{t-g} (T_t - T_g(z)) - N A_p h_{p-g} (T_g(z) - T_s(z)) \quad (5)$$

where the subscripts s and g correspond to the solid and gas phases, respectively. Additionally, subscripts t and p denote a single particle and the inner tube wall. The governing 1-D mass conservation equations for both gaseous species  $\text{O}_2$  and Ar are

$$v(z) \frac{dc_{\text{O}_2}}{dz} = - \frac{\dot{m}_{\text{CeO}_2}}{2AM_{\text{CeO}_2}} \frac{d\delta_{\text{eq}}(p_{\text{O}_2}(z), T_s(z))}{dz} \quad (6)$$

$$v(z) \frac{dc_{\text{Ar}}}{dz} = 0 \quad (7)$$

where  $c$  denotes concentration and  $v(z)$  denotes the gas velocity calculated based on the local gas temperature and the ideal gas law. Note that eqs 4 and 5 are coupled to eqs 6 and 7 through  $T_s(z)$  and  $v(z)$ . The boundary conditions are  $T_s(0) = 300$  K,  $T_g(L_{\text{reac}}) = 300$  K,  $T_t = 1873$  K,  $p_{\text{O}_2}(L_{\text{reac}}) = 100$  ppmv, while  $\dot{m}_{\text{CeO}_2}$ ,  $\dot{V}_{\text{Ar}}$ , and  $d_p$  are the operational parameters taken equal to the experimental conditions. Thermal properties ( $c_p$ ,  $k$ ) of solid and gases were taken from the literature.<sup>34,35</sup>

The modeled particle and gas temperature profiles along the reaction zone are shown in Figure 6a for particle diameters  $d_p = 100$ , 150, and 200  $\mu\text{m}$ . The modeled  $\text{O}_2$  concentration and reaction extent profiles along the reaction zone are shown in Figure 6b for the corresponding particle diameters. Small particles of  $d_p = 100$   $\mu\text{m}$  reached maximum temperatures of 1872 K after only 0.07 m, intermediate particles of  $d_p = 150$   $\mu\text{m}$  needed 0.25 m, while larger particles of  $d_p = 200$   $\mu\text{m}$  reached a maximum 1679 K before exiting the reaction zone. This temperature difference has a large effect on the final reduction extent due to the strong temperature dependence on the thermodynamic equilibrium as seen from Figure 6b.<sup>7</sup> Thus, for the investigated solar reactor geometry ( $L_{\text{reac}} = 0.35$  m,  $D_t = 0.191$  m), particle diameters smaller than 200  $\mu\text{m}$  are required to avoid heat transfer limitations. Since the majority of the cycled particles were larger (c.f., Figures 4 and 5),  $\delta$  was primarily limited by heat transfer.  $T_g$  closely follows  $T_s$  for  $d_p = 100$   $\mu\text{m}$  as a result of their high specific surface area. For a constant  $\dot{m}_{\text{CeO}_2}$ , this surface area decreases with increasing  $d_p$ , resulting in a larger difference between  $T_g$  and  $T_s$ . The reduction extents shown in Figure 6b increase significantly after a particle temperature of 1200 K is reached. An additional increase is observed at the end of the reaction zone where the Ar flow enters. For both particle diameters of 150 and 100  $\mu\text{m}$ , which reach  $T_t$ , the reduction extent is limited by the local  $p_{\text{O}_2}$  resulting from the released  $\text{O}_2$  and the purge flow. For example, for a particle diameter of 150  $\mu\text{m}$  the maximum particle

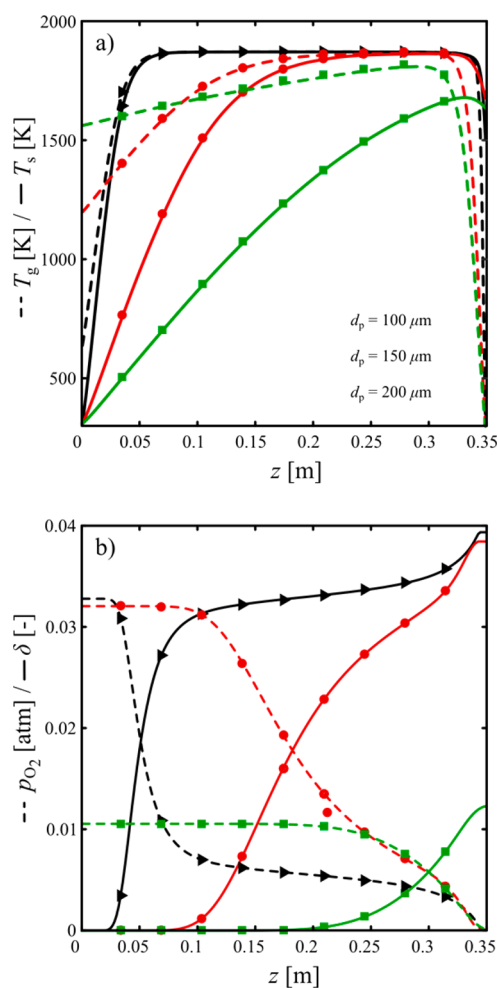


**Figure 6.** (a) Modeled particle temperature profiles ( $T_p$ , solid lines) along the reaction zone for various particle sizes alongside the corresponding gas phase temperature profiles ( $T_g$ , dashed lines). (b) Modeled reduction extent ( $\delta$ , solid lines) and oxygen partial pressure profiles ( $p_{O_2}$ , dashed lines) along the reaction zone. Conditions:  $\dot{m}_{CeO_2} = 100 \text{ mg s}^{-1}$ ,  $\dot{V}_{Ar} = 0.5 \text{ L min}^{-1}$ .

temperature is reached after a distance of 0.3 m while the reduction continues until unfavorable oxygen partial pressures are reached at 0.34 m.

**Experimental Validation.** To further investigate the effect of different operating conditions ( $\dot{m}_{CeO_2}$ ,  $\dot{V}_{Ar}$ , and  $T_t$ ) on reduction extents, particles after cycle 8 were separated using a  $90 \mu\text{m}$  mesh. The resulting particle size distribution had a median diameter of  $152 \mu\text{m}$ , and thus heat transfer limitations were not expected. This batch of particles exhibited no signs of the cohesive nature of the original powder. Again, we subjected this batch to a total of 15 consecutive redox cycles for various  $\dot{m}_{CeO_2}$ . Figure 7 shows  $\delta$  as a function of  $\dot{m}_{CeO_2}$  for  $\dot{V}_{Ar} = 0.25$ , 0.5, 1, and 1.5  $\text{L min}^{-1}$  at  $T_t = 1873$ , and for  $T_t = 1773$ , 1823, and 1873 K at  $\dot{V}_{Ar} = 1 \text{ L min}^{-1}$ . Symbols indicate measured values of  $\delta$ , whereas lines correspond to the modeled  $\delta$  at  $z = 0.35 \text{ m}$  (see Figure 6b). We observed very good reproducibility for  $\delta$  between different cycles which is likely a direct result of the stable particle size distribution and morphology. During this study, the experimental error was  $\pm 5.5\%$ , whereas the experimental error prior to sieving was  $\pm 12.5\%$  (see Figure 3).

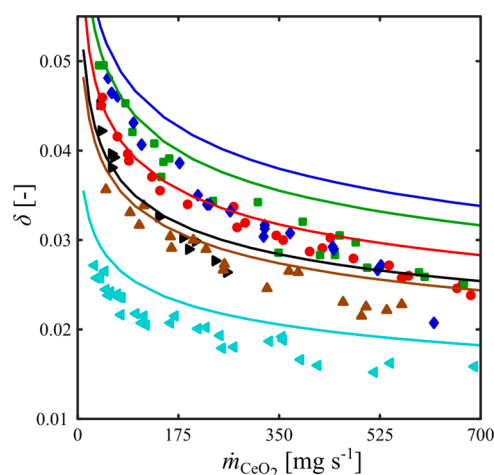


**Figure 7.** Experimentally measured reduction extents as a function of the ceria feeding rate for varying  $\dot{V}_{Ar}$  of 0.25  $\text{L min}^{-1}$  (black  $\blacktriangle$ ), 0.5  $\text{L min}^{-1}$  (red  $\bullet$ ), 1  $\text{L min}^{-1}$  (green  $\blacksquare$ ) and 1.5  $\text{L min}^{-1}$  (blue  $\blacklozenge$ ) at  $T_t = 1873 \text{ K}$  and for varying  $T_t$  of 1823 K (purple  $\blacktriangle$ ), 1773 K (teal  $\blacktriangleleft$ ) at  $\dot{V}_{Ar}$  of 1  $\text{L min}^{-1}$ . Solid lines indicate corresponding results of the heat and mass transfer model.

Independent of the purge flow rate and temperature,  $\delta$  was found to be inversely proportional to  $\dot{m}_{CeO_2}$ . Furthermore, increasing either  $T_t$  or  $\dot{V}_{Ar}$  resulted in higher  $\delta$ , consistent with predictions by the heat and mass transfer model except for high ceria and Ar mass flow rates ( $\dot{m}_{CeO_2} > 175 \text{ mg s}^{-1}$ ,  $\dot{V}_{Ar} = 1.5 \text{ L min}^{-1}$ ). The dependency of  $\delta$  on  $T_t$  was mainly due to thermodynamic equilibrium,<sup>7</sup> while the dependency on  $\dot{m}_{CeO_2}$  and  $\dot{V}_{Ar}$  was mainly a result of the gas phase advection. At constant  $T_t$  and  $\dot{m}_{CeO_2}$ , an increase in  $\dot{V}_{Ar}$  resulted in a decrease of the local  $p_{O_2}$  and, consequently, in higher  $\delta$  according to thermodynamic equilibrium.<sup>7</sup> At constant  $T_t$  and  $\dot{V}_{Ar}$ , the oxygen evolution rate increased with  $\dot{m}_{CeO_2}$ , resulting in a higher local  $p_{O_2}$ . To some extent the gas phase advection limitation can be overcome by operating under vacuum pressures, with the additional benefit of shifting the equilibrium to lower temperatures and eliminating the use of inert gas, while reducing the particle residence time.

At high  $\dot{m}_{CeO_2}$  ( $>175 \text{ mg s}^{-1}$ ), heat transfer is the rate limiting mechanism in the optically thick particle flow. Under such conditions, the modeled  $T_s$  becomes less accurate as the near-transparent media assumption is not fulfilled. The trend that  $\delta$  increases with increasing  $\dot{V}_{Ar}$  observed both experimentally and in the model, suggests that  $\dot{V}_{Ar}$  should be maximized for a given reactor geometry and for the largest particle size while avoiding heat transfer limitations and particle entrainment.

#### 4. CONCLUSION

We have experimentally demonstrated the continuous operation of a solar tubular aerosol reactor for the thermochemical reduction of ceria as part of a two-step redox cycle for splitting  $\text{H}_2\text{O}$  and  $\text{CO}_2$ . The solar reactor featured an alumina tube positioned inside an insulated cavity-receiver and containing countercurrent flows of ceria particles and inert gas to accomplish effective product separation. Solar tests under high-flux irradiation yielded a maximum solar-to-fuel energy conversion efficiency of 0.56% for a single tube, without attempting the recovery of sensible heat of the hot particle and

gas streams. Overall we observed that efficiency increased with both ceria mass flow rate and inert gas flow rate, which affected the residence time, gas phase advection, and heat transfer mainly through the optical thickness. To further probe the physics of the system and cyclability effects, experiments were also performed under well-controlled conditions using an electrically heated tubular reactor. Particle cycling runs revealed a growth of the primary particles from a volume averaged median of 2.44  $\mu\text{m}$  to  $\sim 150 \mu\text{m}$  as a result of sintering, causing a transition from Geldart class C to class A particles and resulting in a gradual decrease of the agglomeration behavior. Specifically, the noncycled powder formed agglomerates with sizes larger than 1 mm, while particles of 150  $\mu\text{m}$  that did not form agglomerates were found after eight cycles, which correlated well with an increase in the reduction extent. A coupled 1-D 2-phase heat and mass transfer model indicated that reduction extents were primarily limited by heat transfer for large particles/agglomerates ( $>200 \mu\text{m}$ ) and by the gas phase advection of product  $\text{O}_2$  for smaller particles. Experiments using ceria particles with a median diameter of 152  $\mu\text{m}$  showed that  $\delta$  decreases with increasing  $\dot{m}_{\text{CeO}_2}$ . In a limited range ( $\dot{V}_{\text{Ar}} < 1.5 \text{ L min}^{-1}$  and  $\dot{m}_{\text{CeO}_2} < 175 \text{ mg s}^{-1}$ ) we additionally observed an increase in  $\delta$  with increasing  $\dot{V}_{\text{Ar}}$  which supports the prediction of the model. We conclude that this tubular aerosol reactor concept requires the selection of appropriate particle sizes that avoid radiative heat transfer limitations and inert gas flows that enhance gas phase advection but avoid particle entrainment.

## AUTHOR INFORMATION

### Corresponding Author

\*Email: [aldo.steinfeld@ethz.ch](mailto:aldo.steinfeld@ethz.ch).

### Notes

The authors declare no competing financial interest.

## ACKNOWLEDGMENTS

Financial support by the European Research Council under the European Union's ERC Advanced Grant (SUNFUELS—No. 320541) is gratefully acknowledged.

## NOMENCLATURE

$A_p$  = particle surface area,  $\text{m}^2$   
 $c_p$  = specific heat,  $\text{kJ kg}^{-1} \text{K}^{-1}$   
 $c_{\text{O}_2}$  = molar oxygen concentration,  $\text{mol m}^{-3}$   
 $c_{\text{Ar}}$  = molar argon concentration,  $\text{mol m}^{-3}$   
 $D_{v50}$  = median particle diameter for volume-based distribution,  $\mu\text{m}$   
 $D_t$  = tube diameter, mm  
 $d_p$  = particle diameter,  $\mu\text{m}$   
 $E_{\text{inert}}$  = energy required to recycle/separate inert gas,  $\text{J mol}^{-1}$   
 $F_{t-p}$  = view factor between tube wall and particle  
 $h_{s-g_2}$  = heat transfer coefficient between particle and gas,  $\text{W m}^{-2} \text{K}^{-1}$   
 $h_{t-g_1}$  = heat transfer coefficient between tube and gas,  $\text{W m}^{-2} \text{K}^{-1}$   
 $\text{HHV}_{\text{H}_2}$  = higher heating value of hydrogen,  $286000 \text{ J mol}^{-1}$   
 $k_s$  = surface reaction rate constant,  $\text{cm s}^{-1}$   
 $L$  = distance between feeder outlet and balance, m  
 $L_{\text{reac}}$  = reaction zone length, m  
 $m_{\text{CeO}_2}$  = mass of ceria, g  
 $\dot{m}_{\text{CeO}_2}$  = mass flow rate of ceria,  $\text{mg s}^{-1}$   
 $M_{\text{CeO}_2}$  = molar mass of ceria,  $172.115 \text{ g/mol}$

$N$  = particle concentration,  $\text{m}^{-3}$   
 $\dot{n}_{\text{inert}}$  = molar flow rate of inert gas,  $\text{mol s}^{-1}$   
 $p_{\text{O}_2}$  = oxygen partial pressure, atm  
 $p_{\text{O}_2, \text{baseline}}$  = residual oxygen partial pressure, atm  
 $\text{ppmv}$  = parts per million volume  
 $P_{\text{solar}}$  = solar radiative power input, kW  
 $\text{SLPM}$  = standard liters per minute, calculated at 273.15 K and 101 325 Pa  
 $T_{\text{cavity}}$  = nominal solar cavity-receiver temperature, K  
 $T_{\text{reduction}}$  = reduction temperature, K  
 $T_{\text{oxidation}}$  = oxidation temperature, K  
 $T_{\text{ambient}}$  = ambient temperature, K  
 $T_t$  = temperature at the inner wall of the reaction tube, K  
 $T_s$  = particle temperature, K  
 $T_g$  = gas temperature, K  
 $\dot{V}_{\text{Ar}}$  = volumetric purge gas flow rate,  $\text{L min}^{-1}$   
 $v$  = gas velocity,  $\text{m s}^{-1}$   
 $z$  = axial coordinate, m  
 $\delta$  = experimentally measured reduction extent  
 $\delta_f$  = final reduction extent  
 $\delta_i$  = initial reduction extent  
 $\delta_{\text{av}}$  = average reduction extent  
 $\kappa$  = optical thickness  
 $\rho_{\text{CeO}_2}$  = ceria density,  $\text{kg m}^{-3}$   
 $\eta_{\text{solar-to-fuel}}$  = solar-to-fuel energy conversion efficiency  
 $\sigma$  = Stefan–Boltzmann constant,  $5.670373e^{-5} \text{ W m}^{-2} \text{K}^{-4}$

## REFERENCES

- (1) Smestad, G. P.; Steinfeld, A. Review: Photochemical and thermochemical production of solar fuels from  $\text{H}_2\text{O}$  and  $\text{CO}_2$  using metal oxide catalysts. *Ind. Eng. Chem. Res.* **2012**, *51* (37), 11828–11840.
- (2) Steinfeld, A. Solar thermochemical production of hydrogen—a review. *Sol. Energy* **2005**, *78* (5), 603–615.
- (3) Chueh, W. C.; Haile, S. M. A thermochemical study of ceria: exploiting an old material for new modes of energy conversion and  $\text{CO}_2$  mitigation. *Philos. Trans. R. Soc., A* **2010**, *368* (1923), 3269–3294.
- (4) Scheffe, J. R.; Steinfeld, A. Oxygen exchange materials for solar thermochemical splitting of  $\text{H}_2\text{O}$  and  $\text{CO}_2$ : a review. *Mater. Today* **2014**, *17*, 341.
- (5) Ackermann, S.; Sauvin, L.; Castiglioni, R.; Rupp, J. L.; Scheffe, J. R.; Steinfeld, A. Kinetics of  $\text{CO}_2$  reduction over nonstoichiometric ceria. *J. Phys. Chem. C* **2015**, *119* (29), 16452–16461.
- (6) Ackermann, S.; Scheffe, J. R.; Steinfeld, A. Diffusion of Oxygen in Ceria at Elevated Temperatures and Its Application to  $\text{H}_2\text{O}/\text{CO}_2$  Splitting Thermochemical Redox Cycles. *J. Phys. Chem. C* **2014**, *118* (10), 5216–5225.
- (7) Panlener, R. J.; Blumenthal, R. N.; Garnier, J. E. A thermodynamic study of nonstoichiometric cerium dioxide. *J. Phys. Chem. Solids* **1975**, *36* (11), 1213–1222.
- (8) Gokon, N.; Takahashi, S.; Yamamoto, H.; Kodama, T. Thermochemical two-step water-splitting reactor with internally circulating fluidized bed for thermal reduction of ferrite particles. *Int. J. Hydrogen Energy* **2008**, *33* (9), 2189–2199.
- (9) Diver, R. B.; Miller, J. E.; Siegel, N. P.; Moss, T. A. Testing of a CRS solar thermochemical heat engine prototype. *ASME Conf. Proc.* **2010**, *2010*, 97–104.
- (10) Diver, R. B.; Siegel, N. P.; Miller, J. E.; Moss, T. A.; Stuecker, J. N.; James, D. L. In *Development of a CRS solar thermochemical heat engine prototype*. 14th Solar PACES International Symposium, March 4–7, 2008, Las Vegas, NV.
- (11) Kaneko, H.; Miura, T.; Fuse, A.; Ishihara, H.; Taku, S.; Fukuzumi, H.; Naganuma, Y.; Tamura, Y. Rotary-Type Solar Reactor for Solar Hydrogen Production with Two-step Water Splitting Process. *Energy Fuels* **2007**, *21* (4), 2287–2293.

- (12) Lapp, J.; Lipiński, W. Transient Three-Dimensional Heat Transfer Model of a Solar Thermochemical Reactor for H<sub>2</sub>O and CO<sub>2</sub> Splitting Via Nonstoichiometric Ceria Redox Cycling. *J. Sol. Energy Eng.* **2014**, *136* (3), 031006–031006.
- (13) Bader, R.; Bala Chandran, R.; Venstrom, L. J.; Sedler, S. J.; Krenzke, P. T.; De Smith, R. M.; Banerjee, A.; Chase, T. R.; Davidson, J. H.; Lipiński, W. Design of a Solar Reactor to Split CO<sub>2</sub> Via Isothermal Redox Cycling of Ceria. *J. Sol. Energy Eng.* **2015**, *137* (3), 031007–031007.
- (14) Ermanoski, I.; Siegel, N. P.; Stechel, E. B. A New Reactor Concept for Efficient Solar-Thermochemical Fuel Production. *J. Sol. Energy Eng.* **2013**, *135* (3), 031002–031002.
- (15) Chueh, W. C.; Falter, C.; Abbott, M.; Scipio, D.; Furler, P.; Haile, S. M.; Steinfeld, A. High-Flux Solar-Driven Thermochemical Dissociation of CO<sub>2</sub> and H<sub>2</sub>O Using Nonstoichiometric Ceria. *Science* **2010**, *330* (6012), 1797–1801.
- (16) Furler, P.; Scheffe, J. R.; Steinfeld, A. Syngas production by simultaneous splitting of H<sub>2</sub>O and CO<sub>2</sub> via ceria redox reactions in a high-temperature solar reactor. *Energy Environ. Sci.* **2012**, *5* (3), 6098–6103.
- (17) Furler, P.; Scheffe, J.; Gorbar, M.; Moes, L.; Vogt, U.; Steinfeld, A. Solar Thermochemical CO<sub>2</sub> Splitting Utilizing a Reticulated Porous Ceria Redox System. *Energy Fuels* **2012**, *26* (11), 7051–7059.
- (18) Furler, P.; Scheffe, J.; Marxer, D.; Gorbar, M.; Bonk, A.; Vogt, U.; Steinfeld, A. Thermochemical CO<sub>2</sub> splitting via redox cycling of ceria reticulated foam structures with dual-scale porosities. *Phys. Chem. Chem. Phys.* **2014**, *16* (22), 10503–10511.
- (19) Scheffe, J. R.; Welte, M.; Steinfeld, A. Thermal Reduction of Ceria within an Aerosol Reactor for H<sub>2</sub>O and CO<sub>2</sub> Splitting. *Ind. Eng. Chem. Res.* **2014**, *53* (6), 2175–2182.
- (20) Maag, G.; Steinfeld, A. Design of a 10 MW particle-flow reactor for syngas production by steam-gasification of carbonaceous feedstock using concentrated solar energy. *Energy Fuels* **2010**, *24* (12), 6540–6547.
- (21) Lichty, P.; Bingham, C.; Weimer, A.; Perkins, C.; Woodruff, B. Rapid High Temperature Solar Thermal Biomass Gasification in a Prototype Cavity Reactor. *J. Sol. Energy Eng.* **2010**, *132* (1), 011012–011012.
- (22) Melchior, T.; Steinfeld, A. Radiative transfer within a cylindrical cavity with diffusely/specularly reflecting inner walls containing an array of tubular absorbers. *J. Sol. Energy Eng.* **2008**, *130* (2), 021013.
- (23) Welford, W.; Winston, R. *High Collection Nonimaging Optics*; Academic Press: San Diego, CA, 1989.
- (24) Petrasch, J.; Coray, P.; Meier, A.; Brack, M.; Häberling, P.; Wüillemin, D.; Steinfeld, A. A Novel 50kW 11,000 suns High-Flux Solar Simulator Based on an Array of Xenon Arc Lamps. *J. Sol. Energy Eng.* **2006**, *129* (4), 405–411.
- (25) Häring, H.-W.; Ahner, C.; Belloni, A. *Industrial Gases Processing*; Wiley-VCH: Weinheim, 2008.
- (26) Takacs, M.; Scheffe, J.; Steinfeld, A. Oxygen nonstoichiometry and thermodynamic characterization of Zr doped ceria in the 1573–1773 K temperature range. *Phys. Chem. Chem. Phys.* **2015**, *17* (12), 7813–7822.
- (27) Geldart, D. Types of gas fluidization. *Powder Technol.* **1973**, *7* (5), 285–292.
- (28) Schiller, L.; Naumann, A. A drag coefficient correlation. *Vdi Zeitung* **1935**, *77* (318), 51.
- (29) Acrivos, A.; Taylor, T. D. Heat and Mass Transfer from Single Spheres in Stokes Flow. *Phys. Fluids (1958-1988)* **1962**, *5* (4), 387–394.
- (30) Modest, M. F. *Radiative Heat Transfer*; Academic Press, 2013.
- (31) Touloukian, Y. S. *Thermophysical Properties of High Temperature Solid Materials. Vol. 4. Oxides and Their Solutions and Mixtures. Part I. Simple Oxygen Compounds and Their Mixtures*; DTIC Document: 1966.
- (32) Whitaker, S. Forced convection heat transfer correlations for flow in pipes, past flat plates, single cylinders, single spheres, and for flow in packed beds and tube bundles. *AIChE J.* **1972**, *18* (2), 361–371.
- (33) Sun, J.; Chen, M. M. A theoretical analysis of heat transfer due to particle impact. *Int. J. Heat Mass Transfer* **1988**, *31* (5), 969–975.
- (34) Chase, M. W. *NIST-JANAF Thermochemical Tables*; American Chemical Society, 1998.
- (35) Riess, I.; Ricken, M.; Nölting, J. On the specific heat of nonstoichiometric ceria. *J. Solid State Chem.* **1985**, *57* (3), 314–322.